



This is a repository copy of *Near-field multi-slice ptychography: quantitative phase imaging of optically thick samples with visible light and X-rays.*

White Rose Research Online URL for this paper:

<https://eprints.whiterose.ac.uk/208495/>

Version: Published Version

Article:

Hu, Z. orcid.org/0000-0001-7306-883X, Zhang, Y., Li, P. et al. (2 more authors) (2023) Near-field multi-slice ptychography: quantitative phase imaging of optically thick samples with visible light and X-rays. *Optics Express*, 31 (10). p. 15791. ISSN 1094-4087

<https://doi.org/10.1364/oe.487002>

Reuse

This article is distributed under the terms of the Creative Commons Attribution (CC BY) licence. This licence allows you to distribute, remix, tweak, and build upon the work, even commercially, as long as you credit the authors for the original work. More information and the full terms of the licence here:

<https://creativecommons.org/licenses/>

Takedown

If you consider content in White Rose Research Online to be in breach of UK law, please notify us by emailing eprints@whiterose.ac.uk including the URL of the record and the reason for the withdrawal request.



eprints@whiterose.ac.uk
<https://eprints.whiterose.ac.uk/>



Near-field multi-slice ptychography: quantitative phase imaging of optically thick samples with visible light and X-rays

ZIYANG HU,^{1,*}  YIQIAN ZHANG,¹ PENG LI,² DARREN BATEY,² AND ANDREW MAIDEN^{1,2}

¹*Department of Electronic and Electrical Engineering, University of Sheffield, Sheffield, S1 3JD, UK*

²*Diamond Light Source, Harwell Science and Innovation Campus, Fermi Ave, Didcot, OX11 0DE, UK*

*zhu9@sheffield.ac.uk

Abstract: Ptychography is a form of lens-free coherent diffractive imaging now used extensively in electron and synchrotron-based X-ray microscopy. In its near-field implementation, it offers a route to quantitative phase imaging at an accuracy and resolution competitive with holography, with the added advantages of extended field of view and blind deconvolution of the illumination beam profile from the sample image. In this paper we show how near-field ptychography can be combined with a multi-slice model, adding to this list of advantages the unique ability to recover high-resolution phase images of larger samples, whose thickness places them beyond the depth of field of alternative methods.

Published by Optica Publishing Group under the terms of the [Creative Commons Attribution 4.0 License](https://creativecommons.org/licenses/by/4.0/). Further distribution of this work must maintain attribution to the author(s) and the published article's title, journal citation, and DOI.

1. Introduction

Over the past decade, a particularly robust and simple form of lens-free coherent diffractive imaging – ptychography [1] – has become widely practiced and experimented with by researchers in various forms of microscopy, from visible light to UV, X-rays and electrons [2–5]. The x-ray imaging community in particular have pioneered the method and it is now implemented at many synchrotron facilities, where it has been effectively employed in a variety of applications, from the identification of chromosome structures [6] to the reverse-engineering of integrated circuits [7]. Ptychography is conceptually very simple: a target sample is illuminated by a coherent radiation beam; the radiation is diffracted, generating an interference pattern which is recorded by a detector placed some distance “down-beam”; the sample is translated through a grid of positions to illuminate different, although substantially overlapping areas, resulting in a dataset comprising many, often many thousands of diffraction patterns; and finally, iterative optimisation algorithms exploit the redundancy introduced by the overlapping illumination areas to reconstruct from the diffraction patterns a complex-valued image, whose amplitude maps the absorption and whose phase maps optical path length variations across the sample.

Ptychography's headline advantage is the ultra-high resolutions it can achieve, reaching deep sub-angstrom levels in the electron microscope [8] and, in combination with tomography [9], hitting isotropic 3D image resolution below 20 nm [10]. These remarkable resolutions are, however, limited to small, optically thin samples, because, like traditional forms of microscopy, ptychography requires that the entire sample thickness lies within the Depth of Field (DoF) of the imaging system; thicker samples cause ptychographic algorithms either to fail completely or to heavily distort the reconstructed image. Several researchers have approximated the maximum sample thickness, T_{max} , to which ptychography can be reliably applied, both theoretically and

experimentally [11–13]. The general relationship they agree on is given by Eq. (1):

$$T_{max} \leq \frac{c\delta_r^2}{\lambda}. \quad (1)$$

Here δ_r represents the image resolution, λ is the beam wavelength and c is a constant, variously reported to have a value from 1 [12] up to 5.4 [13]. Regardless of this scale factor, the thickness limit of Eq. (1) becomes increasingly severe as the target resolution drops. In X-ray ptychography, for example, even at hard x-ray energies T_{max} falls into the 100's of micron range as the resolution goes beneath 100 nm. This trade-off between thickness and resolution poses a particular problem for ptycho-tomography applications aiming to obtain statistically significant amount of data from meaningful sample volumes, for example mapping connections in brain tissue, where neurons only a few tens of nanometers in diameter can extend over hundreds of microns [14,15].

One way to overcome sample thickness constraints in ptychography is to incorporate a multi-slice model into the reconstruction algorithm [11,16]. A multi-slice model approximates the

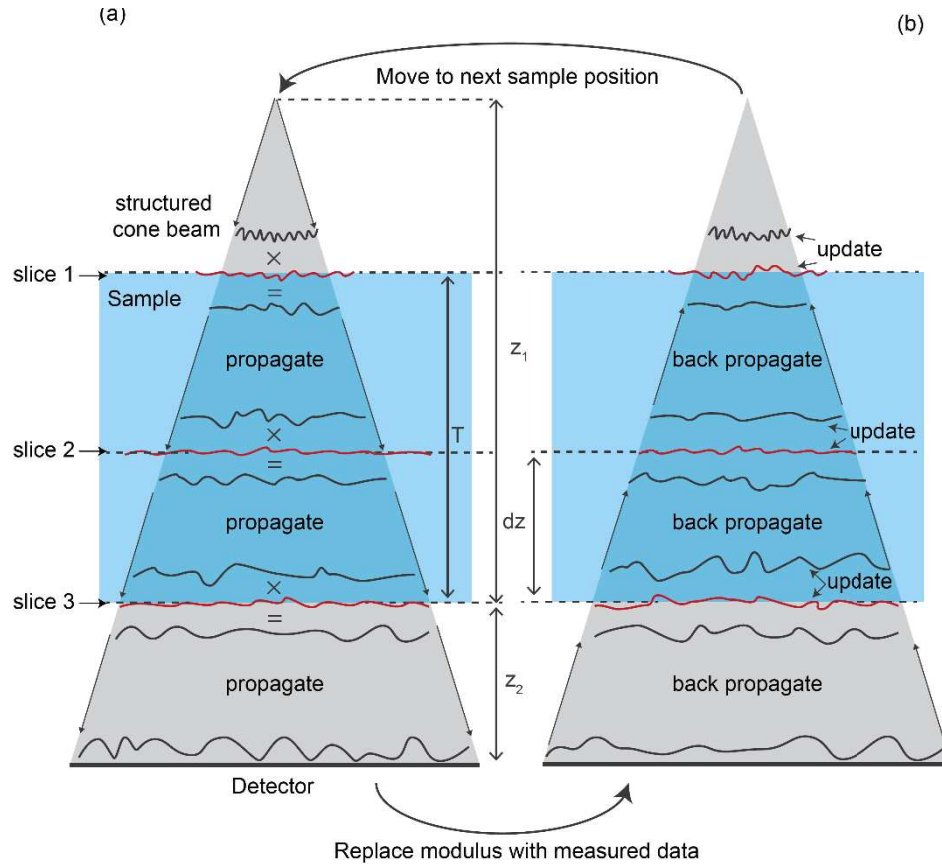


Fig. 1. A schematic illustration of the multi-slice reconstruction process. A sample of thickness T is modelled by thin slices, each of which represents part of the sample volume – the multi-slice algorithm solves for these slices, as well as the illuminating cone beam wavefront. (a) The algorithm first approximates the wavefront incident upon the detector via a chain of multiply-propagate steps through the slices, using current estimates of the illumination wavefront and the slice contents. (b) This wavefront is modified to match the recorded diffraction data and the result then back-propagated through the slices one by one, updating the slice contents and the illumination wavefront at each step.

interaction of a thick sample with a beam of coherent radiation by slicing the sample volume into a series of 2D planes perpendicular to the beam's direction of propagation, as shown in Fig. 1(a). Passage of an X-ray beam through the slices is computed by multiplying the first (most up-beam) slice by the incident illumination wavefront, to model its interaction with that volume of the sample, then propagating, as if through free-space, to the second slice, and so forth in a series of multiply-propagate steps until the final (down-beam) slice is reached. Multi-slice ptychographic algorithms pass estimates of the illumination wavefront and the contents of each slice through this forward model, revise the resulting estimate of the wavefront incident on the detector to agree with the measured data, then reverse the multi-slice process as shown in Fig. 1(b) – back-propagating to each slice in turn and updating the wavefronts and slice contents along the way, via update equations identical to those used in conventional ptychography [17]. For samples whose thickness exceeds that dictated by Eq. (1), the multi-slice model is considerably more accurate than the standard multiplicative approximation used by 2D ptychography, which can be thought of as the reductive case of a multi-slice model with only a single slice. Incorporating this more accurate model within ptychographic algorithms has extended DoF by an order of magnitude, with visible light, X-rays and in the electron microscope [18–22].

To date, the multi-slice method has been applied only in the far-field diffraction regime; our experiments here investigate the application of the multi-slice method to near-field diffraction. Unlike far-field ptychography, where a small, localised patch of illumination is used to ‘probe’ the sample, near-field ptychography utilises a beam modulator, or diffuser, to generate a speckle-like pattern that flood-illuminates the sample [23]. Whilst operating in this near-field regime does not offer the extremely high resolution of the far-field method, it does provide two benefits. First, a large field of view can be captured from data comprising only twenty or so diffraction patterns, compared to many hundreds or thousands for far-field ptychography. (This is especially advantageous for ptycho-tomography, where data collection in the far-field can take many hours.) And second, the dynamic range requirement of the detector can be reduced because there is no huge central diffraction peak in the data. These benefits, and several different experimental configurations for near-field ptychography, have been reported across the wavelength spectrum [24–26].

In this paper, we first introduce an adaptation of the original multi-slice ptychographic algorithm, 3PIE [16], for use in the near-field. We then report results from proof-of-principle experiments using visible light laser illumination, before translating our findings from the optical bench to the I13 coherence beamline at the UK's Diamond Light Source [27].

2. Near-field ptychography using a cone beam

X-ray near-field ptychography was first demonstrated by Stockmar and colleagues [23], who used a cone beam of illumination modulated by a diffuser (a piece of sandpaper) to generate a structured, expanding wavefront incident on a Siemens star test sample, as illustrated in Fig. 2(a). In this geometry, the beam propagates a distance z_1 from the cone apex (at the focus of up-beam optics) to the sample, passes through, and propagates a further distance z_2 to a detector. The detector records the resulting diffraction pattern, which in this regime extends across its entire width, D . As with conventional ptychography, a full near-field ptychographic data set comprises a series of these diffraction patterns, collected over a grid of sample positions; work by Clare *et al.* studied the technique in detail, assessing the effect of diffraction pattern speckle size and different position grids on eventual image quality [28].

The iterative algorithms that reconstruct images from data collected in this cone beam geometry require an appropriate forward model of the experiment, for which these early researchers enlisted help from the Fresnel scaling theorem (FST) [29]. The FST shows that, subject to the paraxial approximation, the cone beam geometry produces data identical to an equivalent experiment where the incident beam is assumed planar, rather than curved, as shown in Fig. 2(b). In this

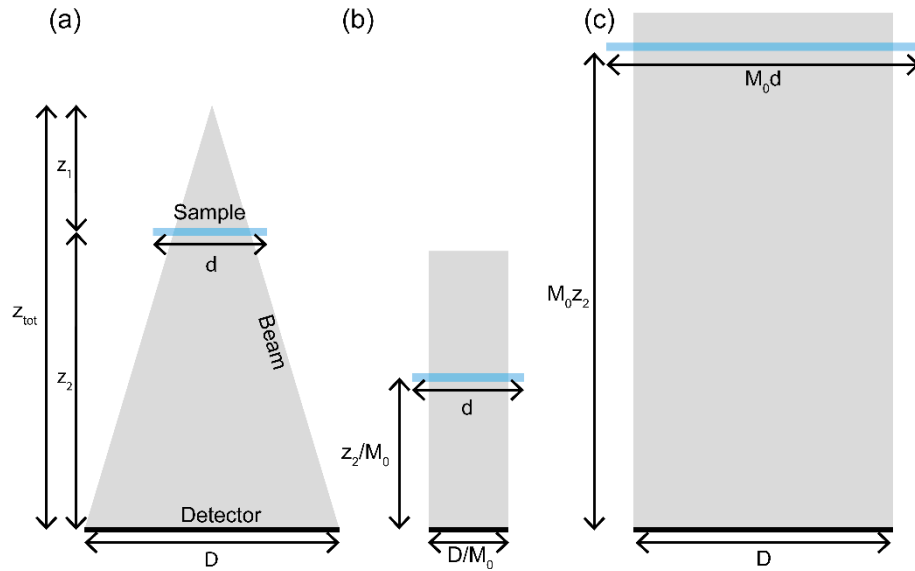


Fig. 2. Two equivalent plane-illumination models for the cone beam geometry. a) the cone beam arrangement: the detector is of width D , d is a representative distance at the sample surface, z_1 is the distance from the cone beam focus to the sample, and z_2 is the distance from the sample surface to the detector. b) provided the small angle approximation is valid, the cone beam can be modelled by an equivalent plane-illumination setup, where the detector is imagined to be smaller and positioned nearer to the sample. Both the detector and the sample-detector distance are scaled down by the geometric magnification, given by $M_0 = \frac{z_1 + z_2}{z_1}$. c) a second entirely equivalent plane-illumination setup imagines the sample-detector distance and the sample itself are scaled up by the same factor, M_0 .

plane-illumination geometry, both the distance from the sample to the detector, z_2 , and the size of the detector, D , are shrunk by the geometric magnification, M_0 , of the cone beam, where:

$$M_0 = \frac{z_1 + z_2}{z_1} = \frac{z_{tot}}{z_1}. \quad (2)$$

This equivalence means that, as far as the reconstruction algorithm is concerned, it is as if the experiment were carried out with a structured, but flat (non-expanding) source of illumination and with a smaller detector placed closer to the sample. This is a straightforward model to implement digitally since it avoids the need to explicitly sample the beam curvature, which can cause aliasing. With the help of the FST, conventional ptychographic algorithms can reconstruct images from cone-beam data with only three minor modifications:

1. Replace the conventional far-field propagation model (a single FFT) with a two-FFT angular spectrum propagator [30],
2. Reduce the propagation distance used in that propagator by a factor of M_0 , from z_2 to $\frac{z_2}{M_0}$,
3. Model the smaller camera by reducing the pixel pitch used in the reconstruction from dc , the real-world pixel pitch of the detector, to $\frac{dc}{M_0}$.

The first of these changes requires some small code changes to the algorithms, but the second and third are pre-processing steps requiring only changes to the algorithm input parameters.

Importantly for our work here, there is a less well-known second equivalent plane-illumination geometry, shown in Fig. 2(c). Here, rather than shrinking the detector, the sample is expanded by

M_0 , and rather than reducing the sample-detector distance, z_2 , it is increased by the same factor: it is now as if the experiment were carried out with a larger facsimile of the sample, placed further away from the detector. This second equivalent geometry requires similar minor adjustments to conventional ptychographic algorithms:

1. Replace the conventional far-field propagation model with the angular spectrum propagator as before,
2. Increase the propagation distance used in that propagator from z_2 to $z_2 M_0$,
3. Use Eq. (3) to convert the scan positions measured from the sample translation stage, $r_{x,y}$ (in metres), to pixel offsets $r_{m,n}$ in the matrix representing the reconstructed sample image:

$$r_{m,n} = \frac{M_0}{dc} r_{x,y}. \quad (3)$$

Again, the first requirement involves small changes to the code whilst the second and third only involve changes to the algorithm input parameters.

There are no computational differences between the two methods of implementing the FST – their propagation kernels and thus their outputted images are identical. Only the frame of reference changes, with the first method using the sample as the reference frame and the second using the detector. This is inconsequential for 2D ptychography, but when it comes to multi-slice ptychography the less well-known method of keeping the detector as the fixed frame of reference, and therefore not having to change the pixel pitch, will prove easier to implement.

3. Multi-slice algorithm for the cone beam geometry

To adapt multi-slice ptychography for the cone beam geometry the FST must be used to propagate not only from the sample to the detector, as in the 2D case discussed in Section 2, but also between the slices in the multi-slice model. This additional deployment of the FST is made complicated by the changing geometric magnification within the sample thickness: the magnification is higher for the up-beam face of the sample, closest to the cone beam focus, decreases within the sample volume, and reaches a minimum at the down-beam face, closest to the detector. Application of the FST must therefore use a slightly larger magnification at the first slice than at the second slice, and so forth. It is possible to do this through an extension of Fig. 2(b) to the multi-slice case [31], but this involves re-interpolating the wavefronts at each slice of the object to accommodate the changing magnifications. Instead, a simpler approach extends Fig. 2(c) to implement the multi-magnification FST, through the equivalence of the two geometries shown in Fig. 3.

Figure 3(b) shows an equivalent three-slice model of the actual experimental geometry in Fig. 3(a), where the slices are located at the down-beam face of the sample, a distance z_2 from the detector; an arbitrary distance dz up-beam from this; and at the up-beam face of the sample, a distance $z_2 + T$ from the detector and a distance $z_1 - T$ from the cone apex. The magnification at the down-beam face is M_0 , given by Eq. (2) as it was for the 2D case. The magnification of the slice located dz meters up-beam of this face is given by Eq. (4):

$$M_{dz} = \frac{z_1 + z_2}{z_1 - dz} = \frac{z_{tot}}{\frac{z_{tot}}{M_0} - dz}, \quad (4)$$

with the magnification at the down-beam slice calculated by substituting $dz = T$.

Within the sample, the z-axis of the model in Fig. 3(b) is stretched non-linearly, such that the physical distance between two adjacent slices in the multi-slice model increases by the product of the magnifications of each slice. For example, illustrated in the Figure are two slices located $z_2 + dz$ and $z_2 + T$ up-beam of the detector. The physical distance between these slices is $T - dz$ and

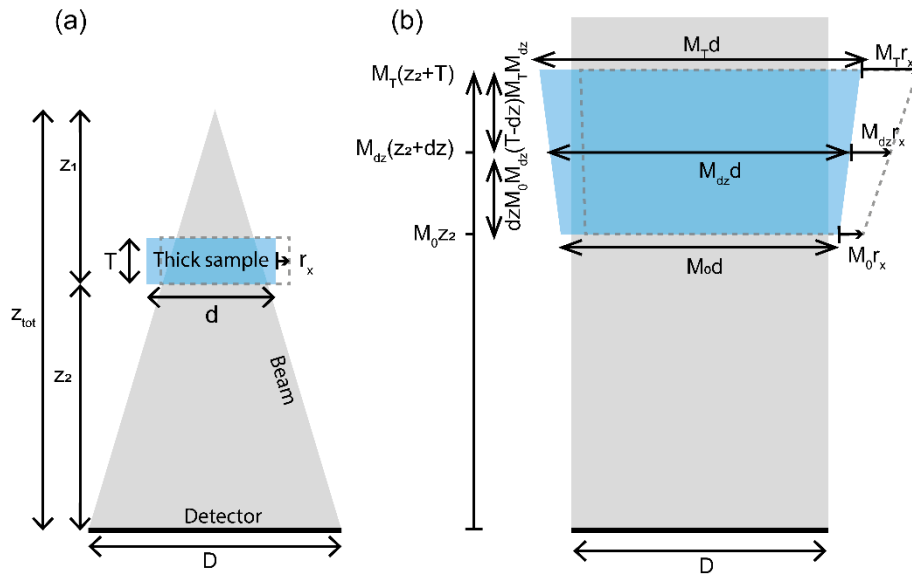


Fig. 3. An equivalent plane-illumination model when the sample is thicker than the depth of field. a) shows the experimental setup, the sample thickness is T , the detector is of diameter D , d is a representative distance on the down-beam face of the sample, r_x is an example sample translation between positions in the ptychographic scan, which moves the sample to the location shown by the dotted line. z_1 is the distance from the cone beam focus to the down-beam face of the sample and z_2 is the distance from the down-beam face to the detector. b) shows an equivalent plane-illumination model for a), incorporating the change in magnification within the sample volume. The distance from the detector to the down-beam sample face is multiplied by the base geometric magnification M_0 . The sample itself is imagined to be stretched both laterally and axially as shown, reflecting the magnification changes within the sample volume. The model incorporates parallax by scaling the ptychographic scan translations by the magnification at different planes, as shown by the translation vectors to the right and the dotted outline.

the magnifications of the slices are calculated from Eq. (4) as M_{dz} and M_T : the model therefore implements the FST by stretching the intervening distance to $(T - dz)M_T M_{dz}$. This model is consistent with the usual 2D near-field model shown in Fig. 2, in that any one of the slices in the model can be chosen and the rest of the slices “deactivated” (maintained as free-space or matrices of ones in the algorithm) and the result is the same as for one of the 2D algorithms, albeit with the propagation to the detector broken into several sub-propagations.

Making use of the equivalence in Fig. 3, similar adjustments to those used to convert conventional 2D ptychographic algorithms for cone-beam near-field data also apply to the multi-slice case. The adjustment steps now are as follows:

1. As with the 2D modifications, use the angular spectrum propagator to propagate from the down-beam face of the sample to the detector,
2. Increase the propagation distance used in that propagator from z_2 to $z_2 M_0$,
3. Multiply the propagation distances between adjacent slices in the multi-slice model by the product of the magnifications of the two slices,
4. Set different magnifications for each slice of the multi-slice model by converting the measured sample positions, $r_{x,y}$, to pixel offsets, $r_{k,m,n}$, that are different for each of the

$k = 1 \dots K$ slices. These offsets are calculated according to Eq. (5):

$$r_{k,m,n} = \frac{M_k}{dc} r_{x,y}, \quad (5)$$

where M_k is the magnification at the plane of the k th slice, given by substituting the corresponding slice position, dz , into Eq. (4).

Again, step 1 requires minor modification of the code, but steps 2-4 are preprocessing steps and only require changes to the input parameters to the 3PIE algorithm; once these pre-processing steps are carried out, the algorithm proceeds exactly as outlined in Fig. 1 and as detailed in the original work [3]; alternative multi-slice ptychographic reconstruction algorithms can also be modified in the same way to accommodate the cone beam geometry [11].

4. Results

4.1. Optical bench experiment and results

As an initial test of the multi-slice, near-field method and of the reconstruction algorithm outlined in Section 3, we carried out experiments on the optical bench setup shown in Fig. 4. Here the cone beam illumination is generated by a collimated laser beam passed through a microscope objective lens, with structure imparted to the beam using a scotch tape diffuser. This structured cone beam illumination wavefront, recovered during the reconstruction process, is shown in the bottom right corner of the Figure. Having passed through the thick sample, the wavefront propagates to the detector, which records diffraction patterns at a series of different sample positions. An example diffraction pattern is shown in the top left corner. The test specimen

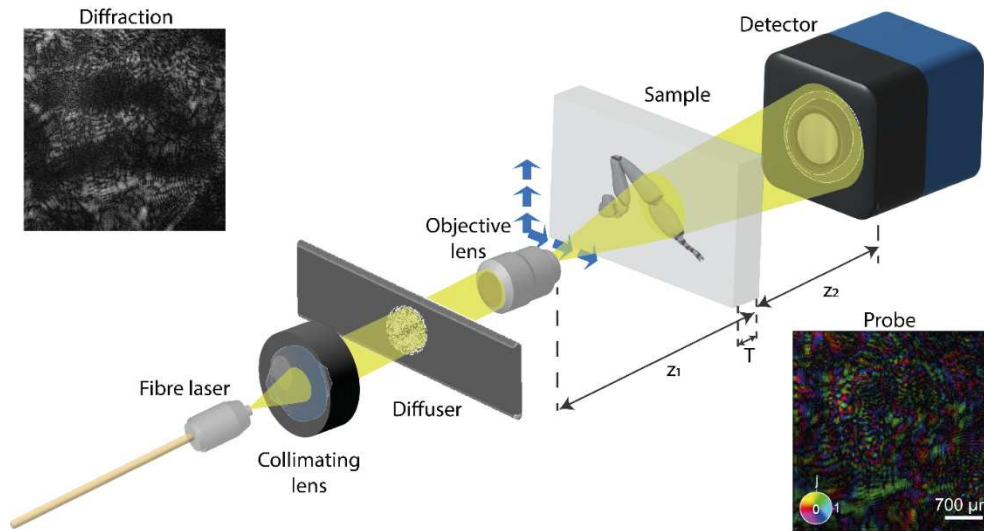


Fig. 4. A multi-slice optical ptychography setup. The beam from a fibre laser passes through a collimating lens, then a diffuser before hitting the inverted objective lens. The objective focuses the beam to a point, and from there the structured wavefront expands as it propagates a distance z_1 to arrive at the sample of thickness T , which is mounted on a motorised translation stage. After passing through the sample the wavefront then propagates a distance z_2 to the detector. An example of a 2048×2048 pixel diffraction pattern collected from the setup is shown top left, and the structured illumination wavefront, recovered during the reconstruction process, is shown bottom right.

in these optical bench experiments was a set of bee's hind legs, approximately $250\ \mu\text{m}$ thick, mounted on a standard optical microscope slide and covered by a coverslip. 100 diffraction patterns were collected using a spiral scan pattern [32] with a linear overlap between adjacent scan positions of 90%. Complete experiment details can be found in the Methods section.

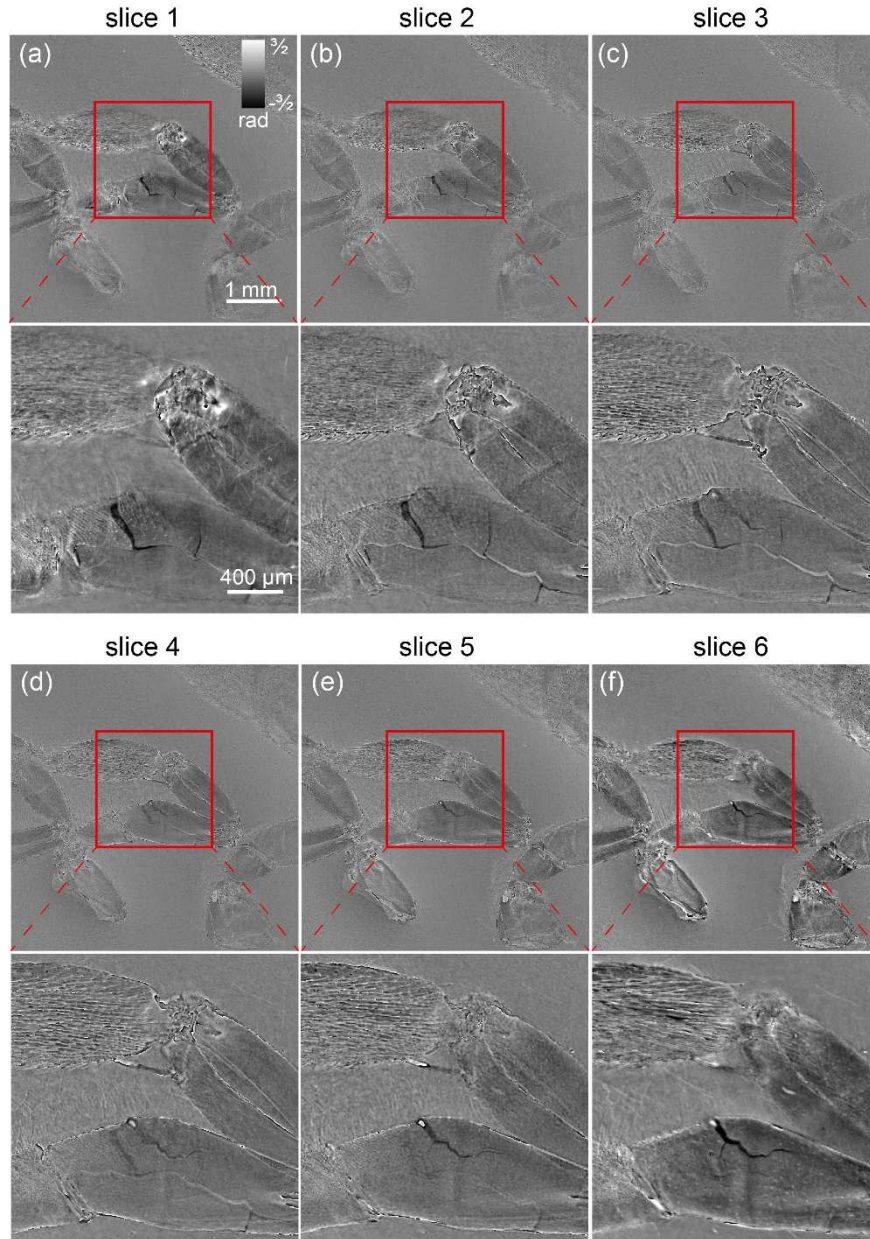


Fig. 5. An example of a 6-layer phase image multi-slice reconstruction using the 3PIE algorithm, the sample is a bee's leg. (a-f) show the slices moving progressively up-beam, from furthest from the camera in (a) to nearest the camera in (f). The lower images in each panel show blow-ups of the areas in the red boxes. The phase ranges have been clipped in these images to enhance contrast.

Feeding the bee leg data from the optical bench setup to the 3PIE algorithm, adapted as set out in Section 3 and using six slices spaced $45\ \mu\text{m}$ apart, produced the reconstruction shown in Fig. 5. Figure 5(a)-(f) show the reconstructed phase images from the six slices: Fig. 5 is up-beam, furthest from the camera, progressing through to Fig. 5(f) closest to the camera. From these images, and the accompanying zoomed-in inset images, it is clear that different features of the bee's leg are separated axially between the slices, indicating that the sample is thick enough to warrant the use of multi-slice ptychography for the reconstruction. This agrees with Eq. (1), which, assuming a best-case image resolution of double the pixel spacing in the reconstruction ($3.61\ \mu\text{m}$), suggests a DoF of between 20-100 μm , depending on the constant c .

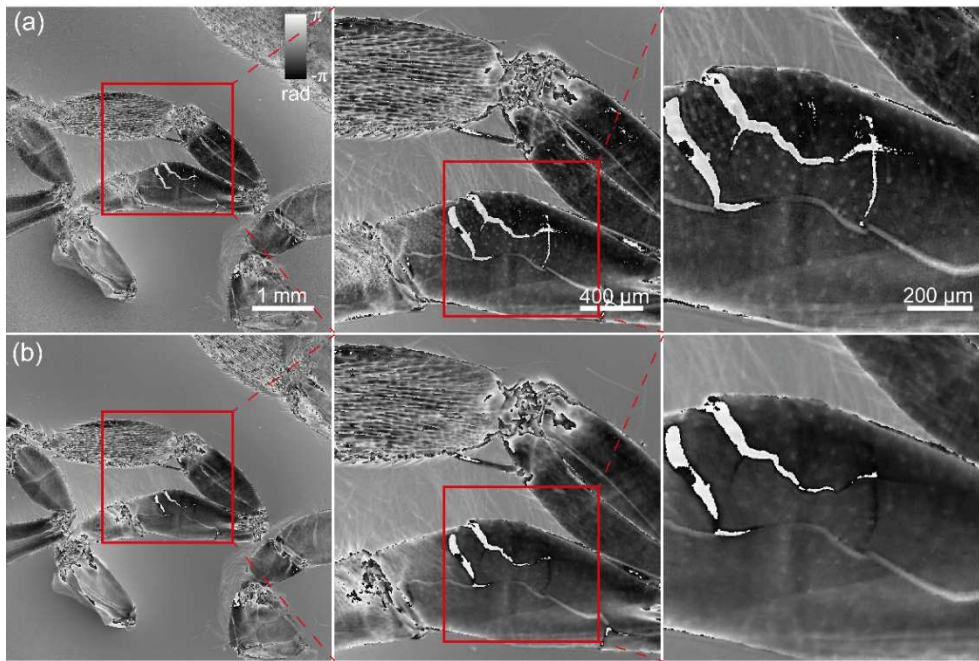


Fig. 6. A comparison of multi-slice and single-slice reconstructions. (a) summed phase of the three slices from the 3PIE reconstruction. (b) comparative single slice phase image.

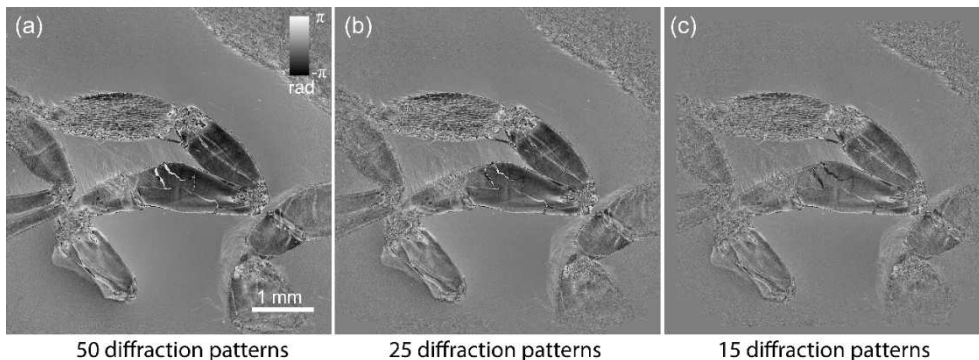


Fig. 7. The summed phase images from 6-layer multi-slice reconstruction of the bee's leg data, using different numbers of diffraction patterns. (a) using 50 diffraction patterns and 500 iterations of the algorithm; (b) using 25 patterns and 1000 iterations; (c) using 15 patterns and 2000 iterations.

To highlight the improvement in DoF of the 3D method compared to conventional near-field ptychography, we combined all six layers of the multi-slice reconstruction together by taking the pixel-wise product of all the slices. (Note: this is effective only if the pixel offsets, $r_{k,m,n}$, for each slice in the reconstruction all share the same mean centre-point, otherwise the slices do not align when the product is taken.) The resulting phase image (the sum of the phases of the six slices) is shown in Fig. 6(a). This phase image is equivalent to a cone beam projection of the sample, where the diffractive, out-of-focus features that would usually be expected for a sample of this thickness have been removed by the multi-slice reconstruction. To highlight this, the phase image resulting from processing the same data using the same algorithm, but employing only a single slice, is shown in Fig. 6(b): although image quality is reasonable here, closer inspection shows that the multi-slice image exhibits much better focus across all features compared to the 2D phase image.

Using the same bee leg data and parameters, we also investigated the minimum number of diffraction patterns required for successful image reconstruction. Since the data were collected using a spiral scan pattern, we reduced the number of patterns by simply discarding the outer loops of the spiral, reducing the number of patterns to 50 (Fig. 7(a)), 25 (Fig. 7(b)) and 15 (Fig. 7(c)). The results show that, for a six-slice reconstruction, effective multi-slice imaging is possible with as few as 15 diffraction patterns. Although considerable noise is introduced at this extreme, and it interesting to note that low spatial frequency content appears to reduce in contrast, potentially as a result of the reduction in field of view for lower numbers of diffraction patterns, the high DoF of the larger scan sizes is retained.

4.2. Multi-slice near-field ptychography using X-rays

X-ray experiments analogous to those conducted on the optical bench were carried out at the I13-1 coherence branch of the Diamond synchrotron in the UK. A schematic diagram of the experimental setup is shown in Fig. 8. The diffuser in these x-ray experiments was a piece of paper, which resulted in diffraction patterns exemplified by the inset in the top left of the figure.

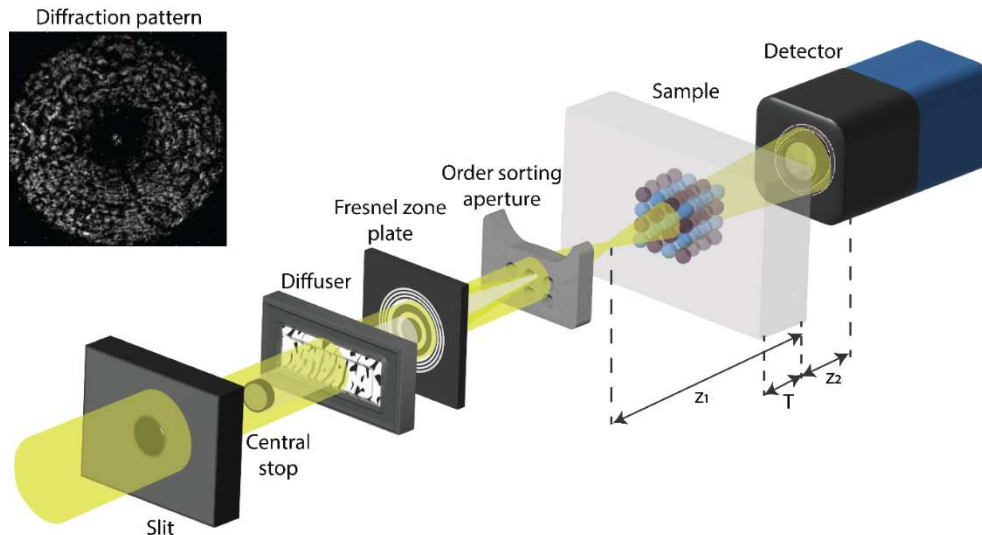


Fig. 8. Experimental set up at the Diamond Light Source I-13 beamline. z_1 is the distance from the zone plate focus to the front of the sample; T is the sample thickness; and z_2 is the distance from the front of the sample to the detector. An example 1024×1024 pixel diffraction pattern from the setup is shown in the top left corner.

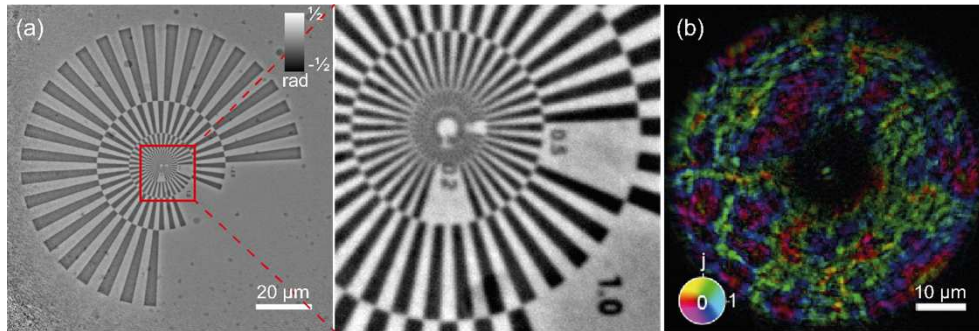


Fig. 9. Results from a calibration experiment of the X-ray near-field setup, using a Siemens star test sample. (a) the reconstructed phase image of the sample, showing also a phase-boosted zoom of the area in the red box. (b) a colour-wheel representation of the reconstructed illumination wavefront, where colour indicates the phase and brightness indicates the amplitude of the reconstruction.

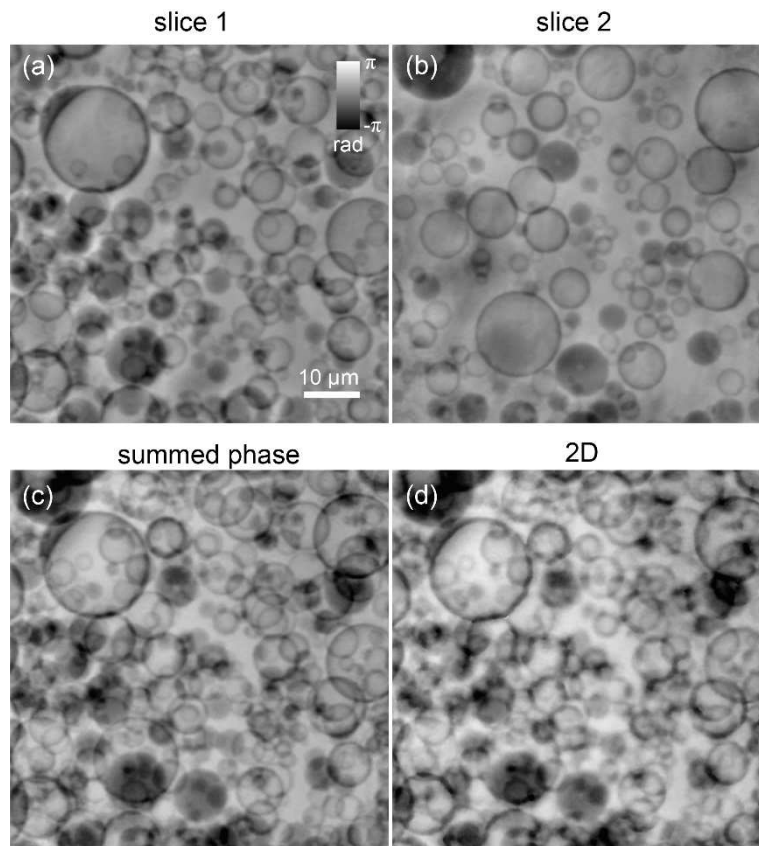


Fig. 10. A 2-layer 3PIE reconstruction of a sample comprising two Kapton films populated with microspheres and separated by a 1 mm airgap. (a) and (b) phase images of the two slices, where (a) is the up-beam plane and (b) is the down-beam plane. (c) pixel-wise sum of the multi-slice layers. (d) the corresponding single-layer reconstruction.

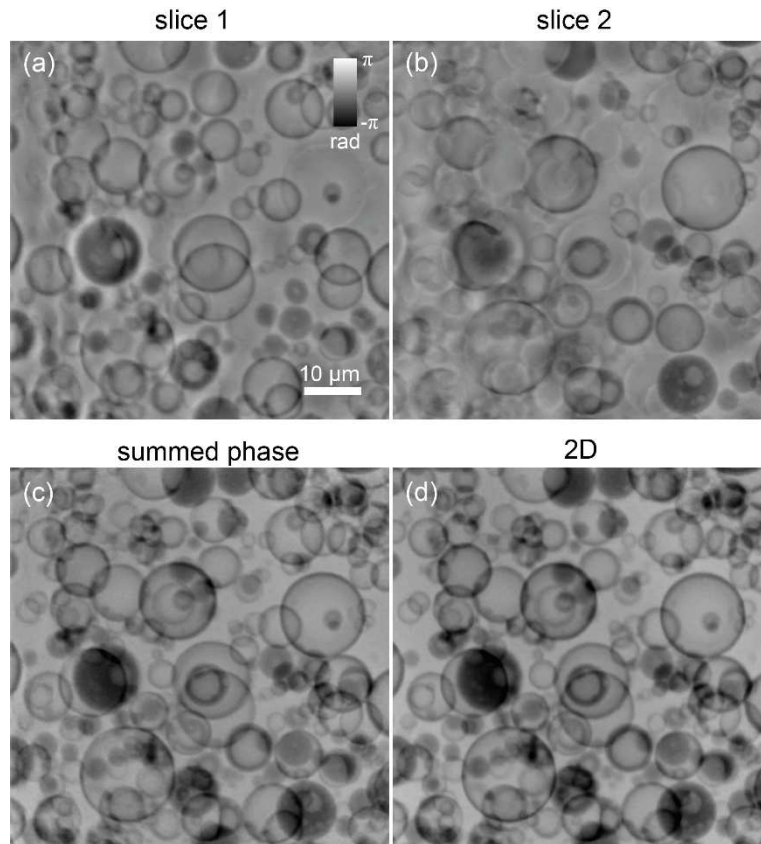


Fig. 11. A 2-layer 3PIE reconstruction of a sample comprising two Kaptan films populated with microspheres and separated by a 0.5 mm airgap. (a) and (b) phase images of the two slices, where (a) is the up-beam plane and (b) is the down-beam plane. (c) pixel-wise sum of the multi-slice layers. (d) the corresponding single-layer reconstruction.

Compared to the optical bench work, the available flux here was lower because of losses in the zone plate and the scintillator, and diffraction data suffered from high noise and low counts (reducing from >10000 per pixel to <1000 per pixel). Diffraction patterns that just filled the detector, and did not extend beyond it, gave the best compromise between flux and field of view. Full experimental details are provided in the Methods section.

A Siemens star sample was used initially to calibrate and optimise our setup. The best phase image from these initial 2D experiments is shown in Fig. 9(a), together with a contrast-boosted zoom-in that indicates a resolution of just below 200 nm. The corresponding reconstruction of the structured cone beam is shown in Fig. 9(b), showing the speckled phase (colour) and amplitude (brightness) introduced by the diffuser and the hollow donut centre resulting from the up-beam central stop.

Having determined from the Siemens star tests the geometry, resolution and magnification ($M_0 = 14$) of the setup, we next replaced the star with various thicker samples. Two double-layer samples were made to test the DoF. The first sample comprised two thin Kaptan film membranes, separated by 1 mm using a metal washer and populated with hollow latex spheres of mixed diameters. Due to the sample's thickness and inaccuracies in its positioning in the beam, the geometric magnification in this experiment was $M_0 = 13.6$, slightly lower than for the Siemens star setup, but data was collected in an identical manner. The 3PIE reconstruction, using two

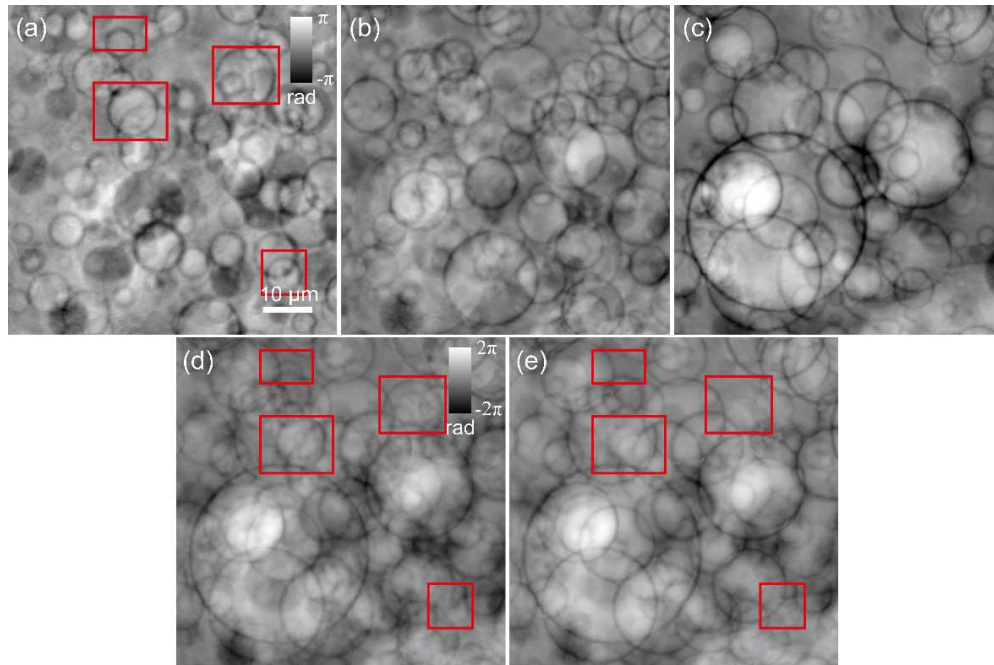


Fig. 12. Reconstruction of microspheres embedded in paraffin, using a three-slice multi-slice model with 1 mm separation between the slices. (a), (b) and (c): Phase images of each slice, where (a) is the upper stream plane (b) is the middle plane and (c) is the down-beam plane. (d) summed-phase projection of the three slices, with phase unwrapped. (e) single-slice reconstruction, with phase unwrapped. The red boxes indicate areas where microspheres have disappeared in the single-slice image.

slices spaced 1 mm apart to match the measured sample properties, is shown in Fig. 10(a)-(d). As shown in Fig. 10(a) and Fig. 10(b), the reconstruction effectively separated the two layers of balls. In fact, clear separation of the spheres is achieved within only a couple of iterations of the algorithm, with full convergence observed after only 50 iterations. The thickness limit dictated by Eq. (1) for this setup, with an X-ray wavelength of 0.124 nm and a resolution of 200 nm, is between 0.31 and 1.6 mm. This indicates that the sample is near the limit of thickness for which 2D ptychography is effective but does not exceed it greatly; the clear depth separation of the two layers is therefore unexpected, something we will discuss further in Section 5.

The two separate layers are combined by pixel-wise multiplication in Fig. 10(c) and for comparison the same dataset reconstructed using only a single slice is shown in Fig. 10(d). Although most features are still present in the 2D image, resolution is reduced considerably and the whole image is blurred, implying that the effective reconstruction plane of the 2D image – which is “chosen” by the algorithm in the sense that it is defined by the concurrent reconstruction of the structured illumination profile – falls somewhere between the two Kaptan film layers. It appears to be a trait of ptychography generally that blind recovery of the probe results in some self-adjustment of the reconstruction plane, to a location that gives a best fit to the measured data.

To test the separation limit of our setup, we used the same method to make a second two-layer Kaptan film sample, this time with a 0.5 mm separation – at the very lowest end of the DoF according to Eq. (1). Diffraction patterns were captured in the same style, with a magnification measured at $M_0 = 13.3$ in this instance. The reconstruction results are shown in Fig. 11. Reasonable separation of the two layers is still apparent in Fig. 11(a) and Fig. 11(b), although the slices now exhibit noticeable cross-talk. These effects cancel each other out in the pixel-wise

multiplication of the two slices shown in Fig. 11(c), to give a well-focussed 2D cone beam projection, but there is now little to distinguish this image from the single-slice reconstruction of Fig. 11(d). Again, the clear depth separation is surprising, given that diffraction of the beam in the space between the two film layers is now minimal, such that 2D ptychography provides a well-focussed image – if diffraction within the sample volume can be neglected, where does the depth information come from? We will discuss this further in Section 5.

We next tested our method on a continuous test sample, made by embedding the same latex microspheres into a 2.5 mm-thick paraffin block. Diffraction data were collected in the same manner, with a magnification of $M_0 = 13.6$ in this instance. We used a 3-slice model to reconstruct this data, where the separation distances were set to 1 mm to ensure the whole sample thickness fell within the DoF of one of the slices. The reconstructed phase images of each slice and the corresponding pixel-wise product of the slices are shown in Fig. 12. The phase images of the three layers are shown in Fig. 12(a)-(c), where Fig. 12(a) is the up-beam layer, Fig. 12(b) is in the middle and Fig. 12(c) is the down-beam layer. Sectioning of the spheres contained in the paraffin into the different slices of the reconstruction is evident in these figures. The pixel-wise product is shown in Fig. 12(d), and whilst the single-slice image of Fig. 12(e) at first glance does not appear to differ greatly from the pixel-wise product, on closer inspection several microspheres, especially those from the slice shown in Fig. 12(a), have all but disappeared from the 2D image (as highlighted in the red boxes).

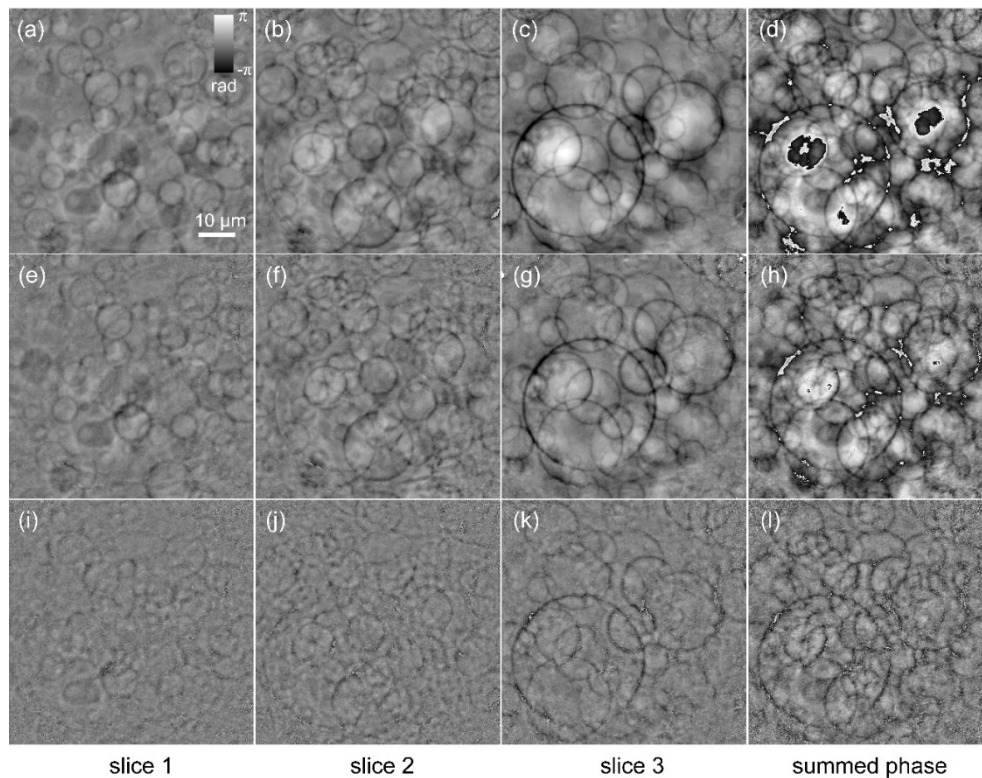


Fig. 13. Phase images of a three slice 3PIE reconstruction with a reduced number of diffraction patterns. (a)-(c) phase images of each slice when using 49 diffraction patterns in a 7×7 grid; (d) summed phase of the three slices; (e)-(g) phase images of each slice when using 36 diffraction patterns in a 6×6 grid; (h) the summed phase; (i)-(k) phase images of each slice when using 25 diffraction patterns in a 5×5 grid; (l) summed phase.

As we did with the optical bench experiments, we investigated the lower limit of diffraction pattern number on the X-ray data. Figure 13(a)-(d) shows that when the diffraction pattern number is decreased from 121 to 49 (a sub-set of the original data created by extracting the central 7×7 scan positions), a relatively high-quality reconstruction is still achieved and there is no significant information loss compared to the larger scan. A further reduction in the diffraction pattern number to 36 still achieves some degree of separation in the slices, albeit with a significant increase in noise. When the number of total diffraction patterns is reduced to 25, the reconstruction starts to fail, especially for the two up-beam slices. Accordingly, the final summed-phase image also shows poor quality. That this lower limit for the X-ray data is higher than it was for the optical bench is not unexpected, given the relative increase in noise and lowering of flux.

5. Discussion and conclusion

On initial inspection, the depth separation achieved in our results appear to contradict Eq. (1) and disagree with the literature on multi-slice ptychography in the conventional, far-field geometry. Indeed, for the results presented in Fig. 11 the inter-slice separation can be set to zero, and the two slices still separate out the microspheres effectively. The cause of this apparent discrepancy is the geometric parallax of the cone beam: it is the way features in different axial locations move relative to one another as the sample scans that dictates the minimum distance between slices for which a degree of depth separation can be obtained. This minimum, T_{min} , is dependent on the change in geometric magnification between slices, as shown in Fig. 14. In the figure, thanks to parallax the star feature, projected onto the plane of the square feature, moves a larger distance as the sample is scanned through the beam. In the extreme case where the star is scanned from one side of the beam to the other, its projection must move at least a resolution element further than the star in order that some depth information be encoded in the recorded data. For this to be the case the star slice must be separated from the square slice by a distance given in Eq. (6):

$$T_{min} = \frac{z_{tot}\delta r}{D} \quad (6)$$

Where D is the diameter of the detector (or of the cone disc if its entirety falls within the detector area), δr is the resolution, and z_{tot} is the distance from the cone beam apex to the detector. Note that this limit is governed by the convergence angle of the cone beam, which under the paraxial approximation is D/z_{tot} , and that it is independent of the wavelength. For the optical bench experiments Eq. (6) gives $T_{min} = 11 \mu\text{m}$, and for the X-ray experiments it gives $T_{min} \approx 100 \mu\text{m}$. These figures are the smallest possible slice separations for which some degree of depth information is encoded in the diffraction data. Equation (6) is applicable only for the highest resolution features in the sample volume and is contingent on the sample being scanned across the entire beam diameter.

In practice, depth separation appears to be some small multiple of the extreme limit in Eq. (6) and is likely sample- and setup-dependent. For the near-field X-ray setup, the minimum slice separation is limited to $\sim 0.5 \text{ mm}$ at an image resolution of $\sim 200 \text{ nm}$, around a factor of 5 above the limit set by Eq. (6). From our results, if the slice separation is lower than this threshold the multi-slice reconstruction does not provide significant benefit over single-slice, 2D imaging, whilst for samples thicker than this, resolution and DoF are improved by using the multi-slice method.

As well as demonstrating a good degree of depth sensitivity and extension of DoF, our work on the optical bench and using coherent hard X-rays has successfully demonstrated multi-slice near-field ptychography over large fields of view using as few as 15 diffraction patterns – a considerable data saving over equivalent far-field ptychographic scans. Future plans include increasing the beam convergence angle (replacing the zone plate with mirrors), investigating different diffusers and their effect on slice separation and image quality, and optimising count

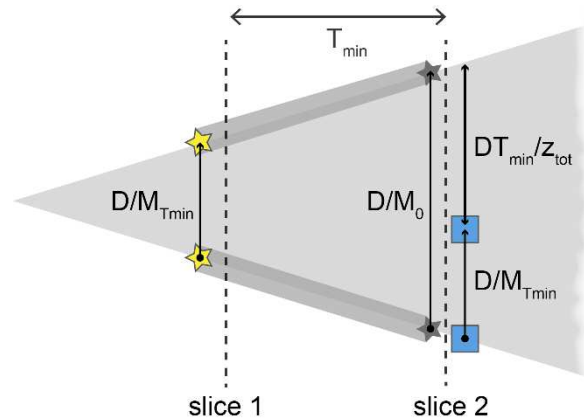


Fig. 14. The minimum separation, T_{min} , for which the recorded diffraction data contains a degree of depth information can be estimated from a simple geometric consideration of parallax. When the sample is translated by a distance D/M_{Tmin} , the star feature moves from one side of the beam to the other. Its projection onto slice 2 initially lines up with the square feature, but after the translation, the square has moved by the translation distance D/M_{Tmin} but the projected star has moved further, a distance D/M_0 . The difference between these two distances is DT_{min}/z_0 and this must exceed the lateral resolution δr if the star and square are to be differentiated in depth. This leads to Eq. (6).

statistics in the X-ray experiments to enable higher resolution and larger fields of view, whilst the addition of modes and other refinements will be incorporated into the reconstruction algorithm. Building on the recent demonstration of multi-slice ptycho-tomography at optical wavelengths [33], we also hope to extend our work here to implement near-field multi-slice ptycho-tomography, aiming to increase accessible sample volume and reduce the huge data sets that are currently required.

6. Experimental methods

6.1. Optical bench setup

Experiments in the visible light regime were conducted on the optical bench setup of Fig. 4. The system comprised a fibre-coupled laser with wavelength of 675 nm (THORLABS S1FC675 5 mW), a collimating lens and a microscope objective (40 \times , 0.75 NA, Olympus); a scotch tape diffuser; a 3-axis linear translation motorised stage from Newport (M-VP-25XL-XYZR); and an sCMOS camera with dynamic range of 16-bit and 2048 \times 2048 pixels on a 6.5 μ m pitch (PCO edge 4.2). The distance between the camera and the focal point of the objective lens was approximately 4.08 cm. The distance between the camera and the sample was 2.98 cm, giving a geometric magnification of $M_0 = 3.6$ and leading to an effective pixel spacing in the reconstruction of 1.80 μ m. Four 0.5s camera exposures were averaged in the recording of each pattern and a dark frame recording was subtracted from the data, with any negative-valued pixels set to zero. The sample was translated through the structured beam in a Fermat Spiral scan pattern [32] with a step size of 130 μ m, equating to an linear overlap between scan positions of 95%.

Image reconstruction used the 3PIE algorithm with the additional steps listed in section 3 – full implementation details of 3PIE are provided in the original paper [16], and MATLAB code is available from Ref. [34]. All images were reconstructed with 500 iterations, with object update coefficient $\alpha = 0.5$ and probe update coefficient $\beta = 1$. The single-slice images were reconstructed using 500 iterations of the same algorithm employing three slices each time, but with only the

middle slice allowed to update. The front and back slices were kept as free-space (unity matrices). The slice separations were set so that the central slice was directly in the middle of the sample volume.

6.2. X-ray experiments

The equipment configuration for the x-ray experiments was as shown in Fig. 8. The beam energy was 9.7 keV corresponding to a wavelength of 0.124 nm. The beam was focused using a Fresnel zone plate with a diameter of 180 μm and outer zone width of 50 nm, resulting in a convergence angle of 2.6 mrad. The intense zero-order beam was eliminated by inserting a gold central stop. A 20 μm order sorting aperture was placed further down-beam of the zone plate. A sheet of paper approximately 1 cm up-beam of the zone plate acted as a diffuser to introduce a structured speckle into the illumination. The detector (a PCO 4000) had a dynamic range of 5455:1 and a pixel pitch of 9 μm . It imaged a scintillator through a microscope objective with a 20 \times magnification. The sample was placed ~ 2.5 cm (z_1) from the zone plate focus and the scintillator was a further ~ 32.5 cm (z_2) down-beam. The resultant geometric magnification, M_0 varied between 13-14 due to slight changes in the sample position and its different thicknesses in the different experiments. Its precise value was determined by trial and error during the reconstruction process. Low counts meant that each diffraction pattern required an exposure time of 15 seconds and was binned by a factor of 2 to 1024×1024 pixels. A dark frame recording was subtracted from the data and any negative-valued pixels set to zero. Due to the changes in geometrical magnification between the different experiments the pixel pitches in the reconstructions ranged from 64–69 nm. All diffraction data were collected using a raster scan with random offsets added to eliminate artefacts that can arise with a periodic grid [32]. We calibrated the step size in the initial Siemens star experiments and achieved best results with a step size of 10 μm (an overlap ratio between scan positions of $\sim 86\%$), plus random perturbations to the regular grid of ± 2.5 μm .

The two-layer sample was fabricated using a mixture of 2–20 μm hollow glass beads blown on Kapton discs and mounted on both sides of washers that were 1 mm and 0.5 mm thick. The continuous sample was made from paraffin wax melted on a hot plate in an aluminium foil container mould at 70 degrees. A mixture of the same 2-20 μm diameter hollow glass beads were gently stirred into the liquid paraffin wax until the mixture was evenly distributed, then the mould was removed from the hot plate to cool down until solid. The paraffin block was afterwards manually trimmed and shaped into a cuboid with 2.5 mm thickness.

All images were reconstructed with 500 iterations of the 3PIE algorithm, with object update coefficient α and probe update coefficient β both set to 1. The 2D ptychography images were reconstructed as for the optical bench data, using three slices, but with the front and back slices held fixed as matrices of ones (representing free-space).

6.3. Aliasing

A useful guide when setting up the near-field experiments can be derived from the Nyquist limit on the quadratic phase used to model the sample-to-detector propagation in Fig. 3(b). This places a limit on the magnification that can be handled without aliasing in the model, given by Eq. (7):

$$M_0 < \frac{Ndc^2}{\lambda z_{tot}} + 1. \quad (7)$$

Here N is the number of rows/columns of pixels on the detector and dc is the detector pixel pitch. For the optical bench setup, this gives, approximately, $M_0 < 4$. For the X-ray setup, it gives $M_0 < 20$. In the original work by Stockmar on near-field ptychography, where the wavelength was shorter and the detector pixels larger, they used a magnification of 24, whilst Eq. (7) gives a maximum magnification of 61.

Acknowledgments. The Authors thank our former colleague Dr. Frederick Allars, now working at the Diamond Light Source, for the enthusiastic discussions. We would like to acknowledge the effort of Ms. Zhaklin P Chalakova from the University of Sheffield, for preparing and providing a variety of samples for testing and for the experiments.

The X-ray experiment was performed on beamline I13 at the Diamond Light Source, Didcot, Oxford, UK, under proposal MG30097.

Disclosures. The authors declare no conflicts of interest.

Data availability. Data and code underlying the results presented in this paper are available in Ref. [34].

References

1. J. M. Rodenburg and A. M. Maiden, "Ptychography," in *Springer Handbook of Microscopy*, (Springer, 2019).
2. A. M. Maiden, J. M. Rodenburg, and M. J. Humphry, "Optical ptychography: a practical implementation with useful resolution," *Opt. Lett.* **35**(15), 2585–2587 (2010).
3. M. D. Seaberg, B. Zhang, D. F. Gardner, E. R. Shanblatt, M. M. Murnane, H. C. Kapteyn, and D. E. Adams, "Tabletop nanometer extreme ultraviolet imaging in an extended reflection mode using coherent Fresnel ptychography," *Optica* **1**(1), 39–44 (2014).
4. F. Pfeiffer, "X-ray ptychography," *Nat. Photonics* **12**(1), 9–17 (2018).
5. L. Zhou, J. Song, J. S. Kim, X. Pei, C. Huang, M. Boyce, L. Mendonça, D. Clare, A. Siebert, C. S. Allen, E. Liberti, D. Stuart, X. Pan, P. D. Nellist, P. Zhang, A. I. Kirkland, and P. Wang, "Low-dose phase retrieval of biological specimens using cryo-electron ptychography," *Nat. Commun.* **11**(1), 2773 (2020).
6. A. Bhartiya, D. Batey, S. Cipiccia, X. Shi, C. Rau, S. Botchway, M. Yusuf, and I. K. Robinson, "X-ray Ptychography Imaging of Human Chromosomes After Low-dose Irradiation," *Chromosome Res.* **29**(1), 107–126 (2021).
7. M. Holler, M. Guizar-Sicairos, E. H. R. Tsai, R. Dinapoli, E. Müller, O. Bunk, J. Raabe, and G. Aeppli, "High-resolution non-destructive three-dimensional imaging of integrated circuits," *Nature* **543**(7645), 402–406 (2017).
8. Z. Chen, M. Odstrcil, Y. Jiang, Y. Han, M.-H. Chiu, L.-J. Li, and D. A. Müller, "Mixed-state electron ptychography enables sub-angstrom resolution imaging with picometer precision at low dose," *Nat. Commun.* **11**(1), 2994 (2020).
9. M. Dierolf, A. Menzel, P. Thibault, P. Schneider, C. M. Kewish, R. Wepf, O. Bunk, and F. Pfeiffer, "Ptychographic X-ray computed tomography at the nanoscale," *Nature* **467**(7314), 436–439 (2010).
10. M. Holler, A. Diaz, M. Guizar-Sicairos, P. Karvinen, E. Färm, E. Härkönen, M. Ritala, A. Menzel, J. Raabe, and O. Bunk, "X-ray ptychographic computed tomography at 16 nm isotropic 3D resolution," *Sci. Rep.* **4**(1), 3857 (2014).
11. E. H. R. Tsai, I. Usov, A. Diaz, A. Menzel, and M. Guizar-Sicairos, "X-ray ptychography with extended depth of field," *Opt. Express* **24**(25), 29089–29108 (2016).
12. M. Stockmar, M. Hubert, M. Dierolf, B. Enders, R. Clare, S. Allner, A. Fehrer, I. Zanette, J. Villanova, J. Laurencin, P. Cloetens, F. Pfeiffer, and P. Thibault, "X-ray nanotomography using near-field ptychography," *Opt. Express* **23**(10), 12720–12731 (2015).
13. M. Du, Z. Di, D. Gürsoy, R. P. Xian, Y. Kozorovitskiy, and C. Jacobsen, "Upscaling X-ray nanoimaging to macroscopic specimens," *J. Appl. Crystallogr.* **54**(2), 386–401 (2021).
14. S. H. Shahmoradian, E. H. R. Tsai, M. G.-S. A. Diaz, J. Raabe, L. Spycher, M. Britschgi, A. Ruf, H. Stahlberg, and M. Holler, "Three-Dimensional Imaging of Biological Tissue by Cryo X-Ray Ptychography," *Sci. Rep.* **7**(1), 6291 (2017).
15. C. Bosch, T. Ackels, A. Pacureanu, Y. Zhang, C. J. Peddie, M. Berning, N. Rzepka, M.-C. Zdora, I. Whiteley, M. Storm, A. Bonnin, C. Rau, T. Margrie, L. Collinson, and A. T. Schaefer, "Functional and multiscale 3D structural investigation of brain tissue through correlative in vivo physiology, synchrotron microtomography and volume electron microscopy," *Nat. Commun.* **13**(1), 2923 (2022).
16. A. M. Maiden, M. J. Humphry, and J. M. Rodenburg, "Ptychographic transmission microscopy in three dimensions using a multi-slice approach," *J. Opt. Soc. Am. A* **29**(8), 1606–1614 (2012).
17. A. M. Maiden, D. Johnson, and P. Li, "Further improvements to the ptychographical iterative engine," *Optica* **4**(7), 736–745 (2017).
18. T. M. Godden, R. Suman, M. J. Humphry, J. M. Rodenburg, and A. M. Maiden, "Ptychographic microscope for three-dimensional imaging," *Opt. Express* **22**(10), 12513–12523 (2014).
19. A. Suzuki, S. Furutaku, K. Shimomura, K. Yamauchi, Y. Kohmura, T. Ishikawa, and Y. Takahashi, "High-Resolution Multislice X-Ray Ptychography of Extended Thick Objects," *Phys. Rev. Lett.* **112**(5), 053903 (2014).
20. H. Öztürk, H. Yan, Y. He, M. Ge, Z. Dong, M. Lin, E. Nazaretski, I. K. Robinson, Y. S. Chu, and X. Huang, "Multi-slice ptychography with large numerical aperture multilayer Laue lenses," *Optica* **5**(5), 601–607 (2018).
21. S. Gao, P. Wang, F. Zhang, G. T. Martinez, P. D. Nellist, X. Pan, and A. I. Kirkland, "Electron ptychographic microscopy for three-dimensional imaging," *Nat. Commun.* **8**(1), 163 (2017).
22. Z. Chen, Y. Jiang, Y.-T. Shao, M. E. Holtz, M. G.-S. Michal Odstrcil, I. Hanke, S. Ganschow, D. A. M. Darrell, and G. Schlom, "Electron ptychography achieves atomic-resolution limits set by lattice vibrations," *Science* **372**(6544), 826–831 (2021).
23. M. Stockmar, P. Cloetens, I. Zanette, B. Enders, M. Dierolf, F. Pfeiffer, and P. Thibault, "Near-field ptychography: phase retrieval for inline holography using a structured illumination," *Sci. Rep.* **3**(1), 1927 (2013).
24. T. Wang, S. Jiang, P. Song, R. Wang, L. Yang, T. Zhang, and G. Zheng, "Optical ptychography for biomedical imaging: recent progress and future directions," *Biomed. Opt. Express* **14**(2), 489–532 (2023).

25. A. L. Robisch, K. Kröger, A. Rack, and T. Salditt, "Near-field ptychography using lateral and longitudinal shifts," *New J. Phys.* **17**(7), 073033 (2015).
26. F. Allars, P. Lu, M. Kruth, R. E. Dunin-Borkowski, J. M. Rodenburg, and A. M. Maiden, "Efficient large field of view electron phase imaging using near-field electron ptychography with a diffuser," *Ultramicroscopy* **231**, 113257 (2021).
27. S. Cipiccia, D. Batey, X. Shi, S. Williams, K. Wanelik, A. Wilson, P. Martin, T. Scott, and C. Rau, "Multi-scale multi-dimensional imaging at I13-coherence branchline in diamond light source," in *AIP Conference Proceedings* 2054, 050005 (2019).
28. R. M. Clare, M. Stockmar, M. Dierolf, I. Zanette, and F. Pfeiffer, "Characterization of near-field ptychography," *Opt. Express* **23**(15), 19728–19742 (2015).
29. D. M. Paganin, *Coherent X-Ray Optics* (Oxford University, 2006).
30. J. W. Goodman, *Introduction to Fourier Optics* (Roberts, 2016).
31. E. R. Shanblatt, Y. Sung, R. Gupta, B. J. Nelson, S. Leng, W. S. Graves, and C. H. McCollough, "Forward model for propagation-based x-ray phase contrast imaging in parallel- and cone-beam geometry," *Opt. Express* **27**(4), 4504–4521 (2019).
32. X. Huang, H. Yan, R. Harder, Y. Hwu, I. K. Robinson, and Y. S. Chu, "Optimization of overlap uniformness for ptychography," *Opt. Express* **22**(10), 12634–12644 (2014).
33. P. Li and A. M. Maiden, "Multi-slice ptychographic tomography," *Sci. Rep.* **8**(1), 2049 (2018).
34. Z. Hu, "Multislice Near-field Ptychography," figshare (2023), <https://doi.org/10.15131/shef.data.21830094>.